POLITECNICO DI TORINO
Repository ISTITUZIONALE

Sensorless direct flux vector control of synchronous reluctance motor drives in a wide speed range including standstill

Publisher copyright

(Article begins on next page)

04 August 2020

Sensorless Direct Flux Vector Control of Synchronous Reluctance Motor Drives in a Wide Speed Range Including Standstill

Arzhang Yousefi-Talouki, and Gianmario Pellegrino, *Senior Member, IEEE*

Abstract -- **This paper proposes a sensorless direct flux vector control scheme for synchronous reluctance motor drives. The proposed controller operates in stator flux oriented coordinates, regulating in closed-loop the amplitude of stator flux linkage and the current component quadrature to flux vector, at constant switching frequency. A hybrid position and speed observer is proposed, covering a wide speed range, based on back-electromotive force (EMF) integration and augmented at zero and low speed levels by high-frequency signal injection. Cross-saturation position estimation error is inherently compensated by the proposed observer scheme. Various experimental results for a 2.2-kW synchronous reluctance motor are presented to verify the feasibility of the proposed method.**

Index Terms--**Direct flux vector control; Sensorless control; Synchronous reluctance motor; Zero speed sensorless control; Cross-saturation.**

I. INTRODUCTION

IN recent years, synchronous reluctance motors (SyRMs) have been widely adopted due to their known cost and efficiency advantages. These motors benefit of low manufacturing cost and simple structure, without windings nor magnets on their rotor [1-4]. The application of SyRMs will presumably grow in the coming years, because of the price uncertainty of rare earth raw materials used in permanent magnets, and because of stricter regulations on motors' efficiency [5]. Moreover, the possibility of encoderless control will facilitate the applicability of the SyRM to a larger number of applications.

The direct torque control (DTC) method possess several advantages respect to conventional current vector control, such as fast torque response and robust implementation [6-8]. In the DTC scheme, electromagnetic torque and stator flux amplitude are closed-loop controlled in the stator reference frame, without requiring the rotor position feedback. In this sense, the DTC is a good and robust sensorless control scheme. At low speed levels, the back-electromotive force (EMF) flux estimation becomes imprecise and more refined flux and position observers schemes are adopted for zero speed sensorless control [8]. The direct flux vector control (DFVC) method presented in [9-11] maintains the main features of DTC as well as features of vector control method such as fixed switching frequency and straightforward limitation of the current vector amplitude. Amplitude of stator flux linkage and the torque current component are the two controlled variables in this scheme. The stator voltage reference components are obtained through two proportional-integral (PI) regulators, in stator flux oriented coordinates, called d_s,q_s. The amplitude of stator flux is controlled directly via the d_s-axis channel, while the torque current component is controlled using the q_s-axis voltage component.

Dealing with the rotor position estimation techniques, sensorless methods are divided into the ones based on back-EMF induced by the rotational movement of the rotor, and the ones based on high-frequency signal injection to track the magnetic saliency of the rotor. The performance of back-EMF based schemes is good above a minimum level of fundamental frequency that can be as small as 1 Hz according to the literature. However, rotor position estimation deteriorates at low speeds and it is impossible under load at standstill, where the motional back-EMF is zero [12-13]. In such low speed range, the position observer is often augmented with signal injection to track the rotor magnetic saliency. In [14] a sensorless direct torque control method was proposed for internal permanent magnet synchronous motor drives. A combined flux observer enhanced with high-frequency signal injection was presented to cover the whole speed range. However, the performance of the drive at standstill was not presented experimentally.

The SyRM is inherently salient and complies well with signal injection-based estimation techniques. In [15] a hybrid active flux-high frequency injection method was proposed for sensorless control of axially laminated synchronous reluctance motor drives. In [16] a back-EMF based position observer combined with high-frequency signal injection was proposed for SyRM drives. However, both methods use a constant current on the d-axis instead of the MTPA control law, to limit the machine's parameters variation with the load torque. In [17], a hybrid active-flux and arbitrary signal injection for SyRMs was proposed. A hysteresis approach was proposed for the transition from the active-flux and signal injection modes. Dealing with direct-flux vector control method, to our best knowledge, there are only a few papers reporting the combination of this method with sensorless applications. In [18], a sensorless direct-flux vector control method was proposed for induction motors, but not at low speeds and standstill.

In this paper, a sensorless direct flux vector control method is presented, operating from zero to maximum speed. The main contribution of the presented method is the combination of a sensorless technique with the direct flux vector control method in the whole speed range. At low speed a high-

A.Yousefi-Talouki, and G. Pellegrino are with the Politecnico di Torino, Department of Energy, Corso Duca degli Abruzzi 24, 10129, Torino, Italy (email: arzhang.yousefitalouki@polito.it, gianmario.pellegrino@polito.it).

frequency signal is injected to the estimated rotor d-axis and the high-frequency component of q-axis flux linkage is extracted and demodulated to estimate the rotor position. The peculiarity of this method is that the injected signal uses rotor (estimated) coordinates, whereas the DFVC uses the flux coordinates. As the speed increases, high-frequency injection is gradually turned off, commuting to the back-EMF based position estimate.

II. THEORETICAL BACKGROUND

A. Synchronous reluctance motor model

The spatial vector reference frames adopted in the paper are introduced in Fig.1: (α, β), (d, q) and (d_s, q_s) stand for stationary frame, rotor flux frame, and stator flux frame, respectively. The voltage equation of the SyRM in the rotor frame dq is as (1), where R_s is the stator resistance, ω is the rotor angular frequency, $\bar{v}_{dq}$ is the stator voltage vector, $\bar{\iota}_{dq}$ the stator current vector, and $\bar{\lambda}_{dq}$ stands for the stator flux linkage vector.

$$\bar{v}_{dq} = R_s \bar{\iota}_{dq} + \frac{d\bar{\lambda}_{dq}}{dt} + j\omega\bar{\lambda}_{dq} \qquad (1)$$

In addition, the electromagnetic torque is expressed as (2) where p is the number of pole pairs.

$$T = \frac{3}{2} \cdot p \cdot (\lambda_d i_q - \lambda_q i_d) \qquad (2)$$

The magnetic model (3), i.e., the current to flux linkage maps can be stored in two 2-D lookup tables to account for saturation and cross-saturation effects.

$$\begin{cases} \lambda_d = \lambda_d(i_d, i_q) = L_d(i_d, i_q) \cdot i_d \\ \lambda_q = \lambda_q(i_d, i_q) = L_q(i_d, i_q) \cdot i_q \end{cases} \qquad (3)$$

Equations (4) and (5) are obtained by transferring the voltage model (1) and torque equation (2) to the stator flux reference frame (d_s, q_s), where δ is the load angle and λ is the amplitude of the stator flux linkage vector.

$$\begin{cases} v_{ds} = R_s \cdot i_{ds} + \frac{d\lambda}{dt} \\ v_{qs} = R_s \cdot i_{qs} + \lambda \cdot (\omega + \frac{d\delta}{dt}) \end{cases} \qquad (4)$$

Torque expression follows from (2), in terms of current and flux components:

$$T = \frac{3}{2} \cdot p \cdot \lambda \cdot i_{qs} \qquad (5)$$

Or in terms of flux amplitude and phase, using $\lambda_d = \lambda \cdot \cos(\delta)$, $\lambda_q = \lambda \cdot \sin(\delta)$:

$$T = \frac{3}{2} p \cdot \frac{L_d - L_q}{2L_d L_q} \cdot \lambda^2 \cdot \sin(2\delta) \qquad (6)$$

B. Direct flux vector control

The block diagram of direct flux vector control scheme is illustrated in Fig.2. As described in [9], the amplitude of stator flux in stator reference frame (d_s, q_s) and the current component quadrature to stator flux (i_{qs}) are the two controlled variables in this method.
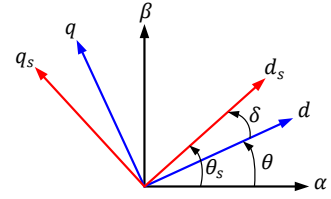

Fig. 1. Reference frames: stator (α, β), rotor (d, q) and stator flux(d_s, q_s) coordinates.

From (4) it can be concluded that the stator flux amplitude (λ) can be regulated by means of d_s-axis of stator voltage. Also, the load angle and consequently torque (6) can be regulated by means of the q_s-axis stator voltage. Alternatively, torque can be controlled by means of current on q_s-axis instead of load angle using the simpler expression (5). Equalizing (5) and (6), i_{qs} is obtained as (7).

$$i_{qs} = \lambda \cdot \frac{L_d - L_q}{2L_d L_q} \cdot \sin(2\delta) \qquad (7)$$

Referring to (4) and using (7), it will be concluded that:

$$\frac{di_{qs}}{dt} = a \cdot (v_{ds} - R_s \cdot i_{ds}) + b \cdot (v_{qs} - R_s \cdot i_{qs} - \omega \cdot \lambda) \qquad (8)$$

$$a = \frac{L_d - L_q}{2L_d L_q} \cdot \sin(2\delta), \quad b = \frac{L_d - L_q}{L_d L_q} \cdot \cos(2\delta) \qquad (9)$$

C. PI Regulators

From (4) it can be seen that the flux amplitude regulation is decoupled from the q_s axis. Flux is regulated through a PI regulator where the bandwidth equals the proportional gain K_{p-ds} [rad/s].

On the other hand, equations (8)-(9) show that closed loop dynamics of i_{qs} is coupled with both control axes, i.e. disturbed by the flux regulating voltage component $v_{ds} - R_s \cdot i_{ds}$. However, this cross coupling disturbance is only visible during flux transients, and those are normally much slower than torque regulation transients. If needed, such voltage term can be model compensated. Going to the tuning of the q_s axis PI regulator, the gain b of the plant in (9) tells that the bandwidth of PI regulator on q_s-axis will be a function of the machine operating points, i.e. will vary with L_d, L_q and δ.

It should be noted that $\hat{\theta}$ and $\hat{\omega}$ in Fig.2 are observed rotor position and rotor speed coming from the position observer which will be described in section III.

D. Stator flux observer

The stator flux observer shown in Fig.3 is a key building block of the proposed control scheme. It is based on the back-EMF integral (voltage model), and includes a compensation signal built after the error between the flux estimates from the voltage model and another flux estimate coming from the current model (flux maps).

Fig. 2. Sensorless direct flux vector control scheme.

The transfer function of the flux observer is as (10) where the scalar gain g (radians per second) is also the crossover speed between the voltage model and the current model flux estimates. As can be seen from (10), when the angular frequency is higher than g, voltage integration prevails, while at lower frequencies the current model dominates. The amplitude and phase angle of the stator flux are the outputs of the flux observer. The flux phase angle ($\hat{\theta}_s = \hat{\theta} + \hat{\delta}$) is obtained by dividing the α, β flux components by the flux amplitude. Fig.4 shows the flux maps of the motor studied in this paper. Other motor data is in Table I.

Fig. 3. Stator flux observer.

Fig. 4. Flux linkage maps of the SyRM under test, evaluated experimentally.

TABLE I - SyR Machine under test specifications

SyR motor	
Rated power/Number of poles	2.2 kW / 4
Nominal Speed/Rated Torque	1500 rpm / 14 Nm
Phase resistance	3.5 Ω
Moment of inertia (J)	$0.005\ kg.m^2$

$$\hat{\lambda}_{\alpha\beta} = \frac{s}{s+g}\left(\frac{v_{\alpha\beta}^* - R_s \cdot i_{\alpha\beta}}{s}\right) + \frac{g}{s+g}\hat{\lambda}_{\alpha\beta,i} \qquad (10)$$

III. SENSORLESS CONTROL SCHEME

This section describes the sensorless control method presented in this paper. Speed is divided into three levels: low speed ([0-50] rpm), medium speed ([50-500] rpm) and high speed (> 500 rpm). From (10) it can be concluded that when the angular frequency ω is approximately three times greater than g, flux observation is fully based on back-EMF integration. In the dual situation, when ω is three times smaller than g or smaller, the current model is alone. In this paper g is set to 35 [rad/s]. Therefore, from [0-~50] rpm, flux observation is based on magnetic model. In the range [50-500] rpm, both current and voltage models contribute to observed flux. For the speeds over 500 rpm, the current model effect vanishes and back-EMF integration model remains alone.

It is well-known that high frequency injection should be dropped out at high speed due to various reasons such as additional core losses, limitation of maximum available voltage vector, etc. In this paper, high frequency signal injection is progressively dropped out between 50 rpm and 100 rpm.

A. High-frequency signal injection method

Operation at zero and near zero speed is obtained with high frequency signal injection and demodulation. Conventionally, a high-frequency excitation voltage is superimposed to the voltage reference signal on the estimated $\hat{d}$-axis direction and the response of the stator current on the $\hat{q}$-axis is measured and imposed to be zero by way of a tracking loop. The rotor position is correct when there is no residual high frequency component on the estimated q-axis. However, it was proved in [19] that using this method, the effect of cross-saturation effect causes the rotor position estimation to be inaccurate and variable with the operating point. Therefore, in this paper, a high-frequency voltage (50 V, 833 Hz) component is superimposed to the estimated rotor $\hat{d}$-axis and the flux component on estimated $\hat{q}$-axis is demodulated in place of commonly used q-axis current component. Therefore, cross-saturation effect is inherently overcome. Fig.5 shows the estimated axis and high frequency injection where ($\hat{d}, \hat{q}$) is estimated rotor reference frame, $\hat{\theta}$ is estimated rotor position, and $\Delta\theta$ stands for position estimation error. u_c is the

amplitude of the injected voltage and ω_c is the carrier frequency.

When a high-frequency voltage is injected into estimated $\hat{d}$-axis, the flux response on estimated $\hat{q}$-axis is as (11), where L_{dd} and L_{qq} are the incremental inductances in d- and q-axis, respectively. $\lambda_{\hat{q}h,i}$ stands for high frequency flux component on estimated $\hat{q}$-axis coming from current model. Multiplying (11) by $\sin(\omega_c t)$, (12) is obtained which after a low pass filter (LPF), an error (ε) is acquired which is position estimation error modulated as can be seen from (13). If ε is forced to zero using a PI regulator, the rotor position is acquired since $\Delta\theta$ becomes zero. Fig.6 illustrates the demodulation process used in this paper, where φ_d is for compensation of discretization delay coming from digital implementation. The tracking loop to obtain the rotor position signal is depicted in Fig.7, where k_ε is as (14). $\hat{\omega}_{HF}$ is the estimated speed obtained from high-frequency injected tracking loop.

$$\lambda_{\hat{q}h,i} = \frac{u_c \sin(\omega_c t)}{\omega_c L_{dd}} \left[\frac{L_{dd}-L_{qq}}{2} \sin(2\Delta\theta) \right] \tag{11}$$

$$\lambda_{\hat{q}h,\varepsilon} = \frac{u_c \sin(\omega_c t)}{2\omega_c L_{dd}} \left[\frac{L_{dd}-L_{qq}}{2} \sin(2\Delta\theta) \right] . [1-\cos(2\omega_c t)] \tag{12}$$

$$\epsilon = LPF(\lambda_{\hat{q}h,\varepsilon}) = \frac{u_c}{2\omega_c L_{dd}} \left[\frac{L_{dd}-L_{qq}}{2} \sin(2\Delta\theta) \right] \tag{13}$$

$$k_\varepsilon = \frac{u_c}{\omega_c L_{dd}} \left(\frac{L_{dd}-L_{qq}}{2} \right) \tag{14}$$

The bandwidth of tracking loop shown in Fig.7 is as (15), where $\omega_{bw,HF}$ stands for the tracking loop bandwidth and $k_{p,HF}$ is the proportional gain of the PI regulator. As can be concluded from (14) and (15), the bandwidth of the tracking loop is proportional to k_ε which itself is dependent on motor operating point. Conventionally the bandwidth of the tracking loop should be three-times less than the low pass filter bandwidth [16].

$$\omega_{bw,HF} = k_\varepsilon . k_{p,HF} < \frac{1}{3} 2\pi \cdot f_{LPF} \tag{15}$$

Fig.8 shows the k_ε for different working points of the motor under test. As can be seen from this figure, the critical area is around $i_q = 0$. However, it should be noted that in the case of synchronous reluctance motors, since there is no magnet, a minimum d-axis saturation current always is needed to ensure both saliency and enough back-EMF for position estimation. Therefore, minimum reference flux (λ^*) has been considered 0.7 [Vs] in this paper. Above this value, reference flux is set based on maximum torque per ampere (MTPA) trajectory as shown in Fig.2. From Fig.4, it can be seen that at no load ($i_q = 0$) condition, 0.7 [Vs] coincides with $i_d = 2$ [A]. Therefore, λ^* setting strategy avoids the critical area as can be seen from Fig.8. As mentioned, k_ε is working points dependent. Thus, k_p and k_i of the PI in tracking loop should be adjusted online to maintain the constant bandwidth. However, in practical implementation, PI can be regulated based on a certain value of k_ε which is in between of no-load and full-load values. Hence, the dependency of PI bandwidth

to different working points can be reduced.

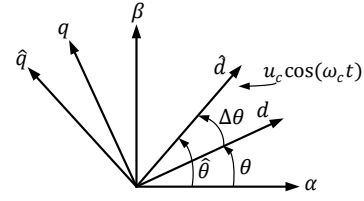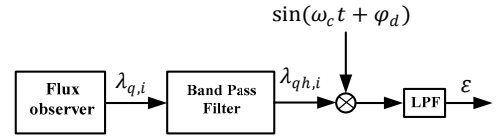Fig. 5. Actual and estimated rotor reference frames.

Fig. 6. High-frequency injection-based demodulation process. φ_d is for compensation of discretization delay.
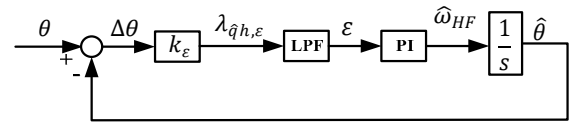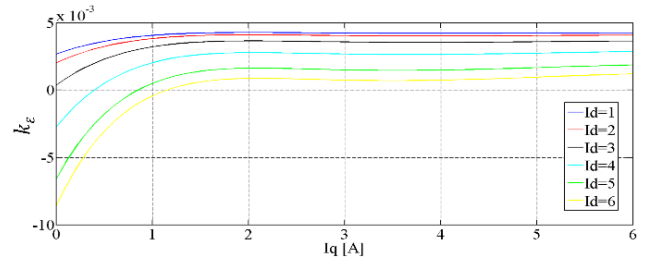

Fig. 7. High-frequency injection-based tracking loop.

Fig. 8. Different values of k_ε dependent on motor working points.

B. Hybrid flux and position observer

Out of the very low speed region (0-50 rpm), rotor position and speed can be estimated using (16) and (17), respectively. For details see [19]. The subscript "F" in (16) and (17) denotes that position and speed come from flux observation.

$$\begin{cases} \sin(\hat{\theta}_F) = \dfrac{\hat{\lambda}_d . \hat{\lambda}_{\beta,i} - \hat{\lambda}_q . \hat{\lambda}_{\alpha,i}}{|\hat{\lambda}_i||\hat{\lambda}|} \\ \cos(\hat{\theta}_F) = \dfrac{\hat{\lambda}_d . \hat{\lambda}_{\alpha,i} + \hat{\lambda}_q . \hat{\lambda}_{\beta,i}}{|\hat{\lambda}_i||\hat{\lambda}|} \end{cases} \tag{16}$$

$$\hat{\omega}_{F,k} = (\sin\hat{\theta}_{F,k} \cos\hat{\theta}_{F,k-1} - \cos\hat{\theta}_{F,k} \sin\hat{\theta}_{F,k-1}).F_s \tag{17}$$

Position estimation based on (16) is combined with the high-frequency injection based method as reported in Fig.9. As can be seen, below 50 [rpm], k is equal to 1. When speed is greater than 50 [rpm], k starts to decrease and from 100 [rpm], high frequency injection will be dropped out completely and the tracking loop will be disconnected from position observer. Also, a pole (h) inserted between $\hat{\theta}$ and $\hat{\theta}_F$ for the sake of smooth transition.
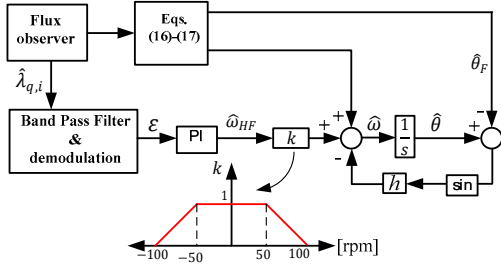
Fig. 9.   Proposed combined rotor position observer.

IV.   EXPERIMENTAL RESULTS

In this section the experimental results for the proposed control strategy will be discussed. The data for the SyRM under test is reported in Table I. the performances of the proposed method is investigated for different speed and torque levels. The sampling and switching period is $T_s = 100\ \mu s$. Below 50 [rpm], 833 Hz high-frequency voltage is injected to the estimated rotor d-axis and above 100 [rpm], high-frequency injection will be stopped. Also, simple compensation method for dead times and power device voltage drops was applied [15]. Actual rotor position and speed are measured using encoder for monitoring purpose. The experimental setup is represented in Fig.11, equipped with a dSPACE 1103 PPC controller board.

A.   Speed control test

In this part the performance of the drive is investigated in speed controlled fashion for low speeds. Fig.11 shows a ± 10 [rpm] step speed reversal where the speed reaches to -10 [rpm] at $t = 5\ s$. The estimated speed, actual rotor speed, flux amplitude, current on q_s- axis, actual and estimated rotor positions, and estimation error are presented in this figure. It can be observed that the performance of the proposed sensorless method is good in both steady state and dynamics.
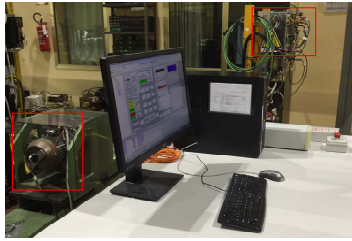
Fig. 10. Experimental test bench: The dSPACE 1103 PPC host computer is on the desk. The SyR motor under test is in the red square to the left. Power converter is in another red square in the right-hand corner.

B.   Torque control test

In this part positive and negative step and ramp torque are applied to the motor at standstill and 50 [rpm] to investigate the performance of the controller. During these tests motor is kept at a constant speed using a servo drive. Figures 12 (a) and (b) show the tests results at standstill where ±12 [Nm] torque is applied at $t = 2\ s$. It can be seen that for both positive and negative step torques, the position estimation error is very close to zero. Also, the performance of the drive can be observed in Fig.13, for ±12 [Nm] step torque command when the rotor speed is kept at 50 [rpm]. Also, at this speed, the
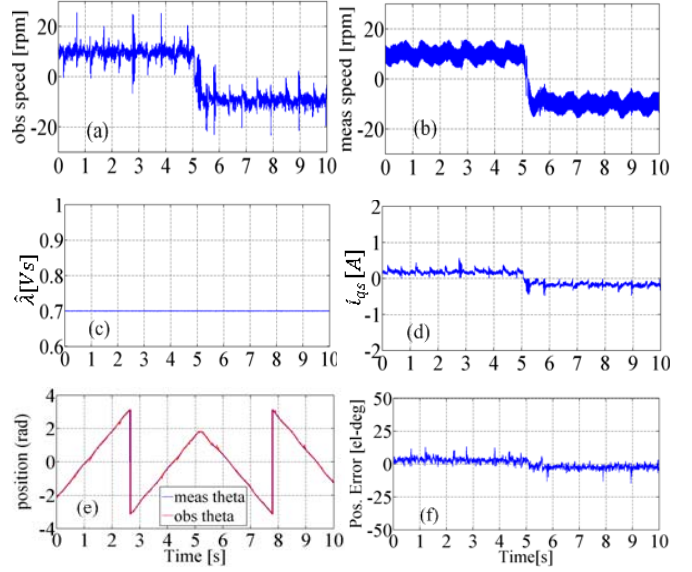
estimation error is close to zero.

Fig. 11. Performance of the controller at low speed ±10 [rpm], (a) estimateded speed, (b) actual speed, (c) amplitude of stator flux, (d) q_s-axis current, (e) estimated and actual rotor position, (f) position estimation error.
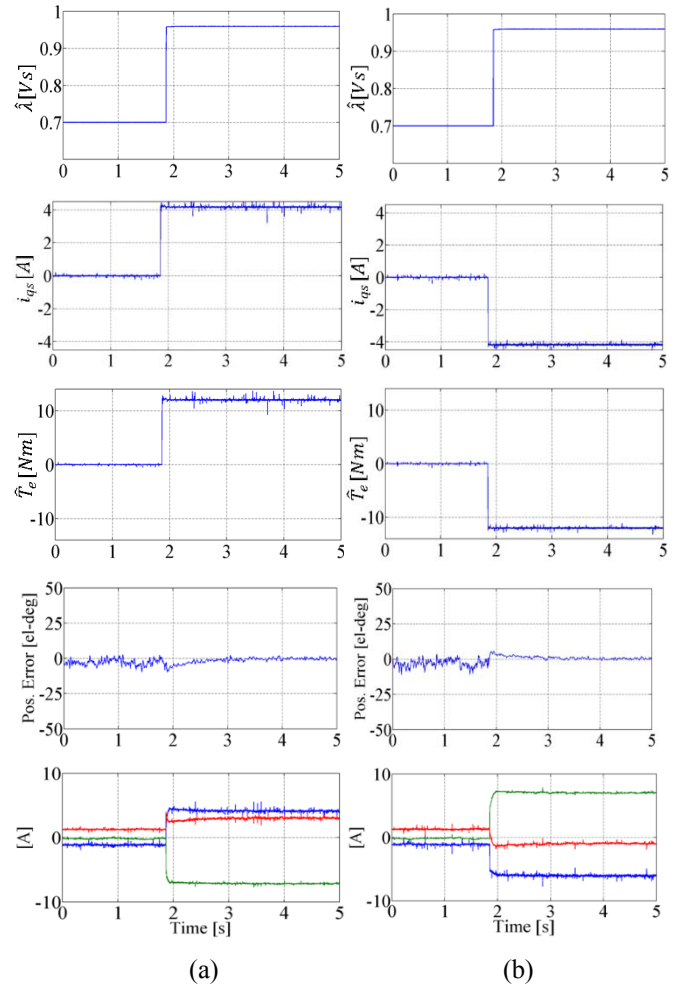

Fig. 12. Experimental results at standstill with ±12 [Nm] step torque, from top to bottom: amplitude of stator flux, q_s-axis current, estimated torque, position estimation error, and three-phase currents; (a) 12 [Nm] step torque, (b) -12 [Nm] step torque.
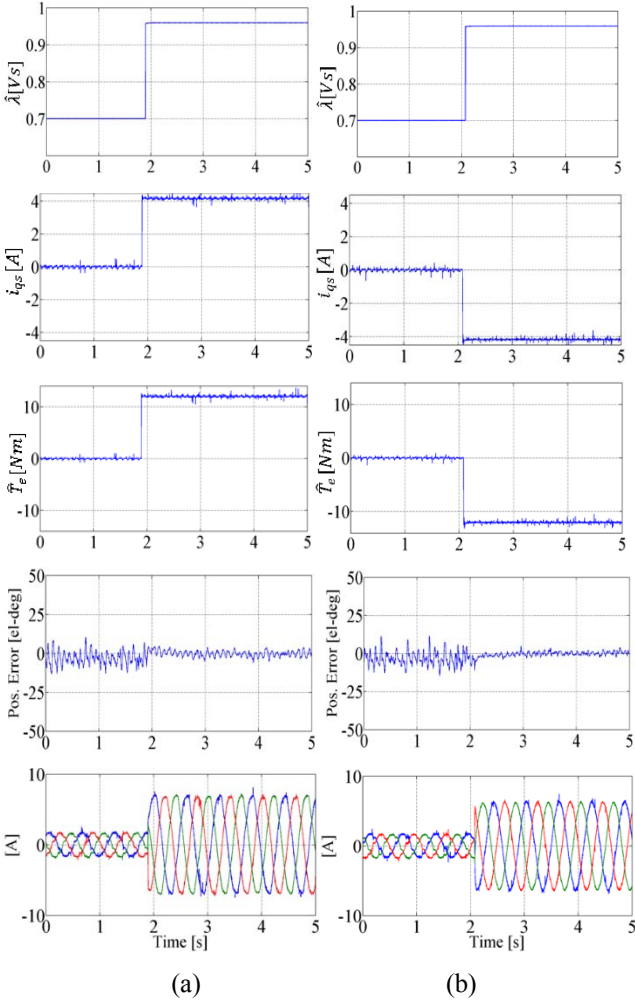
Fig. 13. Experimental results at 50 [rpm] with ±12 [Nm] step torque, from top to bottom: amplitude of stator flux, q_s-axis current, estimated torque, position estimation error, and three-phase currents; (a) 12 [Nm] step torque, (b) -12 [Nm] step torque.

For further investigation of the performance of the proposed controller, ±10 [Nm] ramp torque is applied to the motor at standstill and 50 [rpm]. As described in section III-A, since the demodulation process is done on the q-axis flux component instead of the commonly used q-axis current component, the cross-saturation effect is inherently overcome. This can be seen in figures (14) and (15) when a ramp torque is applied to the motor, the position estimation error is remained close to zero during ramping. Otherwise, if the demodulation process was based on q-axis current component, the position estimation error moves up and down depending the sign of the applied ramp, unless an extra manipulation is done in demodulation process [16].
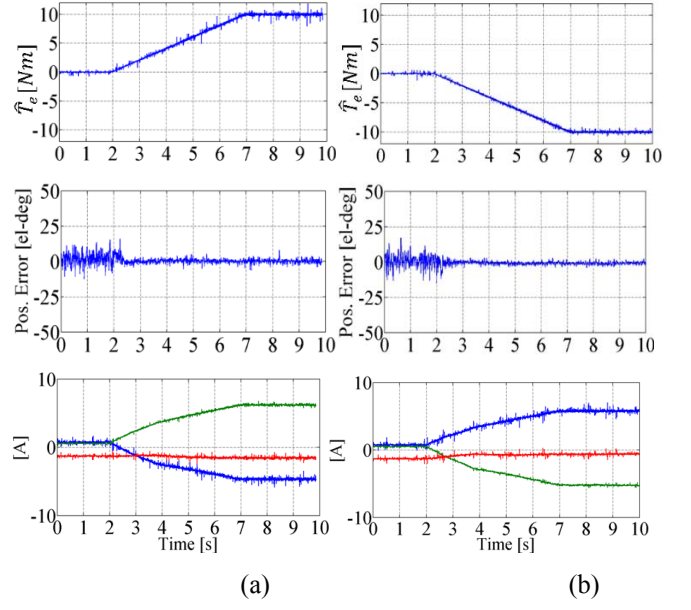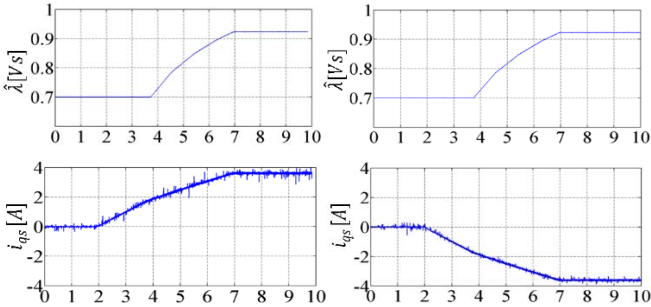

Fig. 14. Experimental results at standstill with ±10 [Nm] ramp torque, from top to bottom: amplitude of stator flux, q_s-axis current, estimated torque, position estimation error, and three-phase currents; (a) 10 [Nm] step torque, (b) -10 [Nm] step torque.
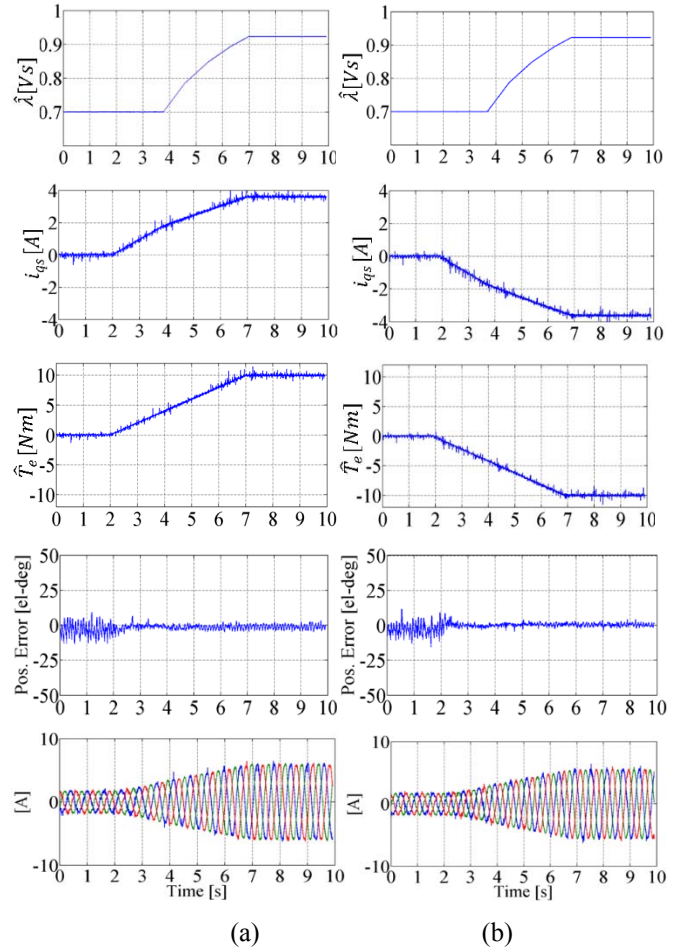

Fig. 15. Experimental results at 50 [rpm] with ±10 [Nm] ramp torque, from top to bottom: amplitude of stator flux, q_s-axis current, estimated torque, position estimation error, and three-phase currents; (a) 10 [Nm] step torque, (b) -10 [Nm] step torque.

V. CONCLUSION

The paper presented a sensorless control method based on direct flux vector control, for synchronous reluctance motor drives. The feasibility of the method was successfully shown through various experimental tests. The performance of the drive has been shown at low speeds with step speed reversal command. Also, the feasibility of the drive was shown when step and triangular torque is applied to the motor. In the whole experimental tests, the rotor position estimation error was close to zero. Moreover, it has been shown experimentally that the position estimation error caused by cross-saturation effect, is cancelled inherently in this presented method.

VI. REFERENCES

[1] Vagati, A.; Pastorelli, M.; Franceschini, G., "High-performance control of synchronous reluctance motors," Industry Applications, IEEE Transactions on , vol.33, no.4, pp.983,991, Jul/Aug 1997.

[2] Boglietti, A.; Cavagnino, A.; Pastorelli, M.; Vagati, A., "Experimental comparison of induction and synchronous reluctance motors performance," Industry Applications Conference, 2005. Fourtieth IAS Annual Meeting. Conference Record of the 2005 , vol.1, no., pp.474,479 Vol. 1, 2-6 Oct. 2005.

[3] Bon-Ho Bae; Seung-Ki Sul, "A novel dynamic overmodulation strategy for fast torque control of high-saliency-ratio AC motor," in Industry Applications, IEEE Transactions on , vol.41, no.4, pp.1013-1019, July-Aug. 2005.

[4] Xinan Zhang; Foo, G.H.B.; Vilathgamuwa, D.M.; Maskell, D.L., "An Improved Robust Field-Weakeaning Algorithm for Direct-Torque-Controlled Synchronous-Reluctance-Motor Drives," in Industrial Electronics, IEEE Transactions on , vol.62, no.5, pp.3255-3264, May 2015.

[5] "Rotating Electrical Machines—Part 30-1: Efficiency Classes of line operated AC motors" (IE-Code), Ed. 1, IEC 60034-30-1, Dec. 2014.

[6] Zhong, L.; Rahman, M.F.; Hu, W.Y.; Lim, K.W., "Analysis of direct torque control in permanent magnet synchronous motor drives," in Power Electronics, IEEE Transactions on , vol.12, no.3, pp.528-536, May 1997.

[7] Inoue, Y.; Morimoto, S.; Sanada, M., "Comparative Study of PMSM Drive Systems Based on Current Control and Direct Torque Control in Flux-Weakening Control Region," in Industry Applications, IEEE Transactions on , vol.48, no.6, pp.2382-2389, Nov.-Dec. 2012.

[8] Foo, G.; Sayeef, S.; Rahman, M.F., "Low-Speed and Standstill Operation of a Sensorless Direct Torque and Flux Controlled IPM Synchronous Motor Drive," in Energy Conversion, IEEE Transactions on , vol.25, no.1, pp.25-33, March 2010.

[9] Pellegrino, G.; Bojoi, R.I.; Guglielmi, P., "Unified Direct-Flux Vector Control for AC Motor Drives," in Industry Applications, IEEE Transactions on , vol.47, no.5, pp.2093-2102, Sept.-Oct. 2011.

[10] Pellegrino, G.; Armando, E.; Guglielmi, P., "Direct-Flux Vector Control of IPM Motor Drives in the Maximum Torque Per Voltage Speed Range," in Industrial Electronics, IEEE Transactions on , vol.59, no.10, pp.3780-3788, Oct. 2012.

[11] Pellegrino, G.; Boazzo, B.; Jahns, T.M., "Plug-in Direct-Flux Vector Control of PM Synchronous Machine Drives," in Industry Applications, IEEE Transactions on , vol.51, no.5, pp.3848-3857, Sept.-Oct. 2015.

[12] Boldea, I.; Paicu, M.C.; Andreescu, G., "Active Flux Concept for Motion-Sensorless Unified AC Drives," in Power Electronics, IEEE Transactions on , vol.23, no.5, pp.2612-2618, Sept. 2008.

[13] Foo, G.H.B.; Rahman, M.F., "Direct Torque Control of an IPM-Synchronous Motor Drive at Very Low Speed Using a Sliding-Mode Stator Flux Observer," in Power Electronics, IEEE Transactions on , vol.25, no.4, pp.933-942, April 2010.

[14] Andreescu, G.; Pitic, C.I.; Blaabjerg, F.; Boldea, I., "Combined Flux Observer With Signal Injection Enhancement for Wide Speed Range Sensorless Direct Torque Control of IPMSM Drives," in Energy Conversion, IEEE Transactions on , vol.23, no.2, pp.393-402, June 2008.

[15] Agarlita, S.-C.; Boldea, I.; Blaabjerg, F., "High-Frequency-Injection-Assisted "Active-Flux"-Based Sensorless Vector Control of Reluctance Synchronous Motors, With Experiments From Zero Speed," in Industry Applications, IEEE Transactions on , vol.48, no.6, pp.1931-1939, Nov.-Dec. 2012.

[16] Tuovinen, T.; Hinkkanen, M., "Adaptive Full-Order Observer With High-Frequency Signal Injection for Synchronous Reluctance Motor Drives," in Emerging and Selected Topics in Power Electronics, IEEE Journal of , vol.2, no.2, pp.181-189, June 2014.

[17] Barnard, F.J.W.; Villet, W.T.; Kamper, M.J., "Hybrid Active-Flux and Arbitrary Injection Position Sensorless Control of Reluctance Synchronous Machines," in Industry Applications, IEEE Transactions on , vol.51, no.5, pp.3899-3906, Sept.-Oct. 2015.

[18] Bojoi, R.; Guglielmi, P.; Pellegrino, G., "Sensorless Stator Field-Oriented Control for Low Cost Induction Motor Drives with Wide Field Weakening Range," in Industry Applications Society Annual Meeting, 2008. IAS '08. IEEE , vol., no., pp.1-7, 5-9 Oct. 2008.

[19] Guglielmi, P.; Pastorelli, M.; Vagati, A., "Impact of cross-saturation in sensorless control of transverse-laminated synchronous reluctance motors," in Industrial Electronics, IEEE Transactions on , vol.53, no.2, pp.429-439, April 2006.

Arzhang Yousefi-Talouki was born in Ghaemshahr, IRAN, in 1985. He received The M.Sc. degree in electrical engineering from Babol University of Technology, Babol, Iran in 2012. He is currently working toward the PhD degree in Politecnico di Torino, Turin Italy. His research interests include electrical machine drives.

Gianmario Pellegrino, (M'06-SM'13) received the M.Sc. and Ph.D. degrees in electrical engineering from the Politecnico di Torino, Turin, Italy, in 1998 and 2002, respectively. He is currently an Associate Professor with the same university. His research interests include the design of electrical machines and the control of electrical drives. He is involved in research projects with industry and has 30 journal papers and one patent. Dr. Pellegrino is an Associate Editor for the IEEE Transactions on Industry Applications. He is the co-recipient of five Prize Paper Awards. He was a visiting scholar at Aalborg University, Denmark, at the University of Nottingham, UK and at the University of Wisconsin-Madison, USA.